

UNCLASSIFIED

Defense Technical Information Center
Compilation Part Notice

ADP014177

TITLE: Validation of Plasma Injection for Hypersonic Blunt-Body Drag Reduction

DISTRIBUTION: Approved for public release, distribution unlimited
Availability: Hard copy only.

This paper is part of the following report:

TITLE: Reduction of Military Vehicle Acquisition Time and Cost through Advanced Modelling and Virtual Simulation [La reduction des couts et des delais d'acquisition des vehicules militaires par la modelisation avancee et la simulation de produit virtuel]

To order the complete compilation report, use: ADA415759

The component part is provided here to allow users access to individually authored sections of proceedings, annals, symposia, etc. However, the component should be considered within the context of the overall compilation report and not as a stand-alone technical report.

The following component part numbers comprise the compilation report:

ADP014142 thru ADP014198

UNCLASSIFIED

Validation of Plasma Injection for Hypersonic Blunt-Body Drag Reduction

J.S. Shang

Center of Excellence for Computing Simulation
Air Vehicles Directorate
Air Force Research Laboratory
2210 Eighth Street
Wright-Patterson Air Force Base
OH 45433-7512, USA

Summary

The optimum blend of numerical and physical fluid experiment for risk and cost reduction is an actual reflection of the stage of maturation for individual technology development. As an illustration, the detailed validation of drag reduction technique using plasma injection was investigated using a side-by-side experimental and computational approach. The major portion of the reduced drag is found from the favorable counter-flow jet shock interaction and thermal deposition.

Introduction

Improving aerodynamic performance of air vehicles via drag reduction has been steadily pursued since the days of the Wright brothers. In high-speed flight, the need of significant drag and heat load reduction for a better performance becomes even more critical. In an assessment of aeronautical science for the future, one realizes that the air vehicle design has fallen into an evolutionary process because the technical innovation is limited to aerodynamics [1]. However, Sear et al pointed out as early as the later 50's, an added new physical dimension of magneto-aerodynamic interaction would revolutionize the performance of high-speed flight [2-5]. Collectively, they demonstrated that electromagnetic force could significantly alter the aerodynamic behavior in plasma media. Therefore, the large volume of magneto-aerodynamic research from Russia in the 80's has stirred a great amount of interests [5-8]. In this interdisciplinary endeavor, at least three independent science disciplines; aerodynamics, quantum chemical kinetics, and electromagnetics are interwoven. In addition, the air plasma (more precisely the weakly ionized air) always associated with an extremely high temperature state, which is a common occurrence in hypersonic flow. This flight environment is not always duplicable in a ground testing facility [9]. Therefore it is essential that the physical-based computing simulation capability be developed if the advantage of a favorable magneto-aerodynamic interaction is to be harnessed for hypersonic flight.

The possible contributors to drag reduction via plasma injection are widely speculated. It is commonly accepted that the counter-flow jet-shock interaction, non-equilibrium thermodynamic state of highly excited international degrees of freedom, and the electromagnetic force could play significant roles. The interdisciplinary phenomenon is extremely difficult to investigate alone by either experimental or computational simulation because each can yield only a partial answer. Also not all observations can be verified independently. Thus, the present investigation resorts to a combination approach.

Optimum blends of numerical and physical fluid experiments span a very wide range of variations for the purposes of validation and calibration of modeling and simulation capabilities. For an interdisciplinary technology development where the aerodynamics, electromagnetics, and quantum chemical physics are integrated both physical and numerical experiments are facing challenges. The synergetic effects to minimize risk therefore are uncertain. In the present effort, a computational and experimental side-by-side investigation on plasma injection for hypersonic blunt-body drag reduction is presented.

Systematic pursuit is guided by hypotheses on physical mechanisms that can generate a favorable magneto-aerodynamic interaction - the counter flow jet shock aerodynamic interaction, the non-equilibrium thermodynamic and chemical phenomenon, and the electromagnetic-aerodynamic interaction. Three-dimensional and axisymmetric, mass-averaged Navier-Stokes equations were solved for counter-flow jet shock interaction. The experimental investigation of the plasma injection was conducted in a nominal Mach 6 open jet, blow-down tunnel. The weakly ionized, counter-flow jet generated by a plasma torch has an electron temperature around 20,000 K, and electron number density greater than $3 \times 10^{12}/\text{cm}^3$.

Experimental Facility

The counter-flow plasma jet and shock interaction is investigated in a blow-down, open-jet, high Reynolds number wind tunnel. At the stagnation temperature of 610 K and a range of stagnation pressures from 3.44 10^2 to 1.40 10^4 kPa, the air stream sustains a uniform test section from the nozzle exit plane and a diameter of 203 mm at the Mach number of 5.8. The mass flow rate of the tunnel spans a range from 0.77 to 4.63 kg/s. For the present investigation, the tunnel is operated at the lowest density of 0.012 kg/m^3 at the free stream pressure of 2 Torr and static temperature of 79 K. Under this operational condition, the Reynolds number is 45,200 per meter.

The force-measuring model is a hemispherical cylinder, which has a nose radius and a total length of 38.1 and 203.2 mm respectively. The model was fitted with three nozzles ($D_t = 2.44, 1.5, \text{ and } 1.27$ mm) to accommodate the plasma torch. However, the drag data is collected only from the nozzle with the throat diameter of 1.27 mm. At the stagnation pressure and temperature of 344.7 kPa and 294 K, respectively, the exit Mach number is 3.63 and yields a mass flow rate of 0.001 kg/s. The nozzle flow changes from over- to under-expanded condition at the stagnation pressure of 1,077 kPa.

The aerodynamic force is measured by a set of 3 piezoelectric force sensors or load cells. The model is isolated from the support strut by these load cells to receive the total axial aerodynamic force exerted on the model. In this arrangement, the wave drag, skin friction drag, and the base drag are not separable but measured together [14,19].

A plasma cutting torch with the PAK Master 50XL power supply and the PCH/M-28 torch supplies the ionized air the counter-flow jet. The maximum power output from this plasma torch is rated at 35 Amp by an AC input single-phase voltage 208. However in the present application, this unit is strictly operated in the starting mode. Therefore, the power output is far below the rated value. The arc starting circuit has a high frequency generator that produces an AC voltage from the 5 to 10 kV at a frequency of approximately 2 MHz. This frequency is far beyond the spectra range of oscillatory drag measurement (up to 5 kHz) for interference. In fact, the basic oscillatory behavior of both air and air plasma is similar, and the predominant oscillatory mode occurs around 100Hz.

The properties of air plasma, such as the electron density and temperature of the air plasma, were measured by a double Langmuir probe. The probe is constructed from a 0.5 mm platinum wire with a double-hole ceramic sleeve and a wire separation distance of 1.0 mm. The sensing area of each probe tip is limited to 2.1 mm^2 . A 100 V Keppco bipolar power supply provides the applied electric potential. Meanwhile, a variable resistor in the circuit has an operable range from 75 to 1,000 Ohms to enable the electric current measurement in microampere range.

Counter-Flow Jet

There is a great deal of literature on the jet-spike or counter-flow jet [10-14]. A number of investigations focused on the aspect of thermal protection. The rest concentrated on the understanding of this intricate flow field structure [10-12]. The counter-flow jet issued from a blunt body in supersonic regime has two distinct states. At the lower injecting pressure, the jet displaces the bow shock upstream. The displaced shock envelope is generally conical and the flow field is unsteady [12,13]. At higher injecting pressures, the

displaced shock actually retracts back from the conical to a blunter configuration and the oscillatory motion ceases. The basic flow field structure is depicted in Figure 1.

The driving force of this interaction mechanism is the expanding jet into a low stagnation pressure shock layer, and then the jet is stagnated by a Mach disk. The jet reverses its direction downstream as a free shear layer. A part of the jet stream is also entrained to form a toroidal recirculating zone beneath the free shear layer. At the reattachment point of the free shear layer to the blunt body, it induces a series of compression waves coalescing into a reattachment ring shock. The counter-flow jet interaction with the bow shock replaces the single wave to a triple shock structure [14]. This multiple shock structure degeneration is the major contributor of wave drag reduction for the plasma injection.

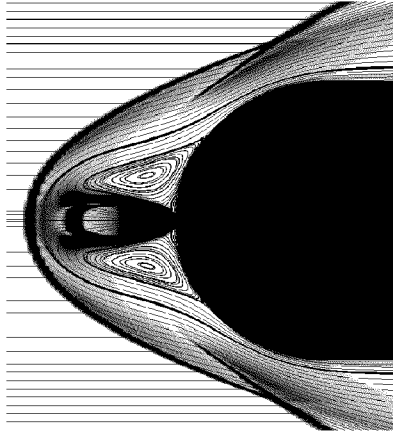


Figure 1. The streamline trace of the jet spike flow field

The shock bifurcation was also discovered by the side-by-side computational and experimental study of the jet spike [14]. At the bifurcation point between the steady and unsteady states, the drag reduction also attains the maximum value. The bifurcation is the consequence of breakdown of the subsonic upstream feedback loop between the Mach disk and the unsteady free shear layer [15]. As the jet injecting pressure increases, the subsonic region connecting the Mach disk and the free shear layer diminishes in size. At the bifurcation point, a part of the supersonic jet actually diverts from the Mach disk and effectively cuts off the feedback loop from the free shear layer and the oscillatory fluid motion ceases. The Mach number contours of the distinct dynamic states astride the bifurcation point are given in Figure 2.

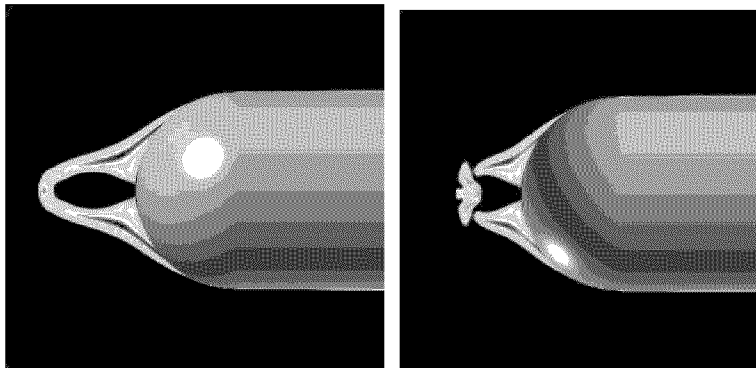


Figure 2, Subsonic Mach number contours of the steady and oscillatory states

An implicit, unstructured Navier-Stokes equations solver, Cobalt [16] was used exclusively to obtain all numerical results. The basic algorithm is that of the Godunov's Riemann formulation coupled with implicit time stepping to yield a second-order spatial and temporal accuracy. The cell-centered, finite-volume

approach can accommodate either the tetrahedron or the hexahedron in three-dimensional space. The governing equations are discretized by the implicit approximation as;

$$[3(\mathbf{U}^{n+1} - \mathbf{U}^n) - (\mathbf{U}^n - \mathbf{U}^{n-1})] / 2 \Delta t + \nabla \cdot \mathbf{F} = 0$$

Where the \mathbf{U} 's are the conservative dependent variables $\mathbf{U}(\rho, \rho u, \rho v, \rho w, \rho e)$ and \mathbf{F} 's are the flux vectors of the Navier-Stokes equations. The reconstruction of the flux vectors at the cell faces is by a least-square approximation.

$$\mathbf{q}_{i \pm 1/2} = \mathbf{q}_i \pm \mathbf{r} \cdot \nabla \mathbf{q}_i$$

Where \mathbf{q} is the vector of primitive variables $\mathbf{q}(\rho, u, v, w, p)$ at the centroid of cell i , $\nabla \mathbf{q}_i$ is the gradient vector and \mathbf{r} is position vector from the centroid to the cell faces.

An outstanding feature of the unstructured grid approach is also derived from the neighbor-cell connectivity of its formulation. The cobalt exhibits an exceptionally scalable, parallel computing performance on all multi-computers using a message passing interface (MPI) library [17]. On an IBM SP3 32-node computation, the data processing rate is 5.28×10^{-6} sec per cell per time step versus a value of 4.22×10^{-5} on a 4-node computation. This parallel efficiency exhibits a nearly linear performance over the range of operations.

In the present application, the no-slip velocity components and adiabatic temperature conditions are imposed on the blunt body surface. For the plasma torch, the sonic throat is prescribed as the entrance boundary for the conical injecting nozzles. The unperturbed free stream condition is specified at the upstream boundary and the no-reflection condition downstream for the far field. The Spalart-Allmaras one-equation model is adopted to achieve the turbulent closure [18].

The computational error is assessed by generating solutions on consecutively refined grid density immediately adjacent to the shock waves. For an embedded conical nozzle in the hemispherical cylinder with a throat diameter of 2.44 mm and exit diameter of 4.70 mm, the exit Mach number is 2.86. Numerical solutions at a free stream Mach number of 5.80 on three grid systems of 185,484, 256,824, and 303,804 were obtained. After the second grid density refinement, the numerical results are essentially grid independent. The identical process was also applied to nozzles of smaller throat diameter ($D_t = 2.5$ and 1.27 mm).

In Figure 3, the first validation of the measured and computed results in the form of schlieren images is presented for the nozzle with a throat diameter of 2.44 mm and the injecting to tunnel stagnation pressure of 0.75 ($P_j/P_0=0.75$). Under this condition, the blurred schlieren photograph reveals the oscillatory flow field structure. For the long-exposure photograph, the blurred image band actually defined the extremes of shock movements. However, the computed schlieren image is limited to a single event in time, and in general has a shorter penetration length in comparison with experimental observations. The resultant shock wave system exhibits two oscillatory frequencies at 100 and 435 Hz. However, the lower frequency oscillation has a dominant magnitude over the others.

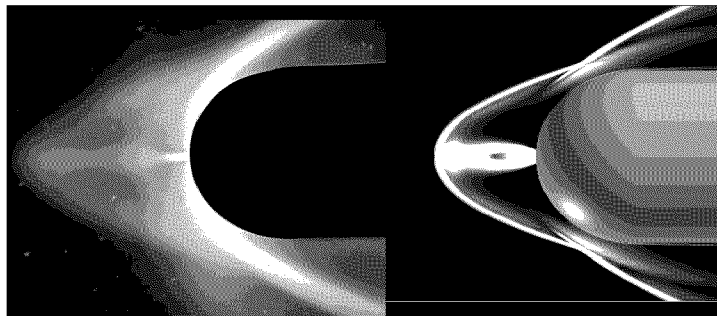


Figure 3. Comparison of Schlieren with computational result at $P_j/P_0=0.75$

The comparison of schlieren with computed result at an injecting pressure beyond the bifurcation point is depicted in Figure 4. The specific comparison is made for the injecting to the tunnel stagnation pressure of

1.05 ($P_j/P_o = 1.05$). At this injecting pressure, the shock wave system jumps to a nearly steady state. The schlieren photograph yields a sharper image than the highly unsteady motion at the lower injection pressure domain. In this figure, the Mach disk that terminates the forward motion of the counter-flow jet, the coalesced reattachment ring shock is clearly exhibited. Even the slipstream originating from the intersection of the bow shock and the ring shock is clearly visible. Both the measured and computed standoff distance of the bow shock shows an identical value of $\Delta/r = 0.744$. The agreement of the overall flow field structure between the experimental and computational results is excellent.

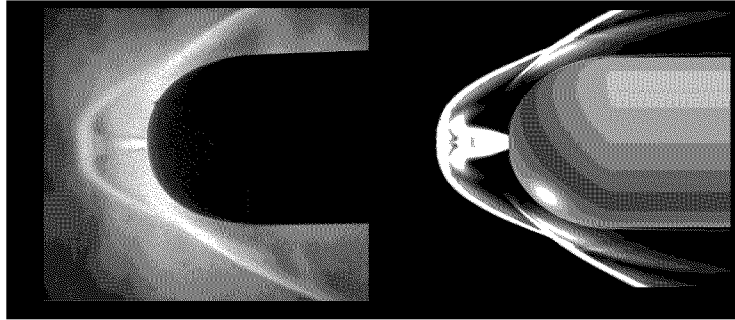


Figure 4. Comparison of Schlieren with computed result at $P_j/P_o = 1.05$

In Figure 5, the more critical verification of experimental data and the computational result of drag is given. In this graph, the normalized drag coefficient of the blunt body with the counter-flow jet is depicted with respect to the pressure ratio of injection and tunnel stagnation pressure. The drag coefficient is normalized by the drag of the same blunt body at the identical flow condition. Two different wind tunnel stagnation pressure conditions are presented at the tunnel stagnation pressures of 50 and 100 psi (0.344×10^3 and 0.688×10^3 kPa). The calculated drag includes the base drag correction from experimental measurements. The base drag evaluated from two pressure taps on the model base region yields a nearly constant value over the entire injection pressure range. A reasonable agreement is noted over the entire tested range including the bifurcation. The numerical results also capture the oscillatory force behavior at both tunnel stagnation conditions. However, the numerical results also predicted pressure bifurcation value lower than experimental observation. Nevertheless, the computational error and experimental data scattering band are estimated from 1.7 to 5.1%.

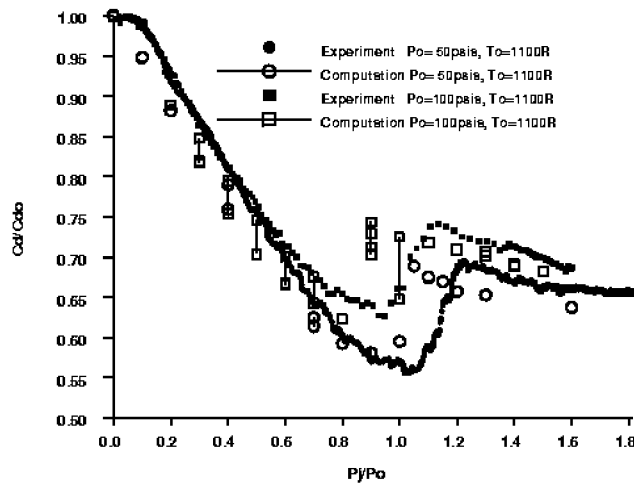


Figure 5. Verified measured and computed drag for blunt body with counter-flow jet

From both experimental observations and computational results, the wave drag reduction for blunt body by a counter-flow jet can be substantial. The reduced drag is mostly derived from the degeneration of a single

bow shock wave to a multiple structure. The amount of drag reduction is strongly dependent on the relative mass flow rate of the oncoming stream versus the injection, the jet exit Mach number, and the specific heat ratio, γ of the injectant (or the chemical composition of the injectant)[12,13]. For the present investigation of the counter-flow jet, the drag reduction increases as the stagnation pressure of the tunnel is decreased to reflected the effect of the higher relative mass flow rate to the drag reduction. This behavior is clearly demonstrated by both computational results (Figure 5) and experimental measurements.

Four sets of normalized drag coefficients with respect to the blunt body data without injection are presented as a function of stagnation pressure ratios of tunnel and the counter-flow jet (P_j/P_0) in Figure 6. The tested wind tunnel stagnation pressures varies from $344.7 \cdot 10^3$ to $2,068.4 \cdot 10^3$ kPa, the maximum drag reduction reaches a value of 40% at the bifurcation point at the lowest wind tunnel stagnation pressure. The drag continuously decreases over the entire tested stagnation pressure range despite the steady rising of the reverse thrust. Associated with the large amount of drag reduction, there is also an abrupt change of dynamic states across a shock bifurcation point. When the injecting pressure or more appropriately the injecting mass flow rate is less than a critical value, the jet-shock interaction will initiate an oscillatory flow motion through the feedback loop of the free shear layer instability [14,15].

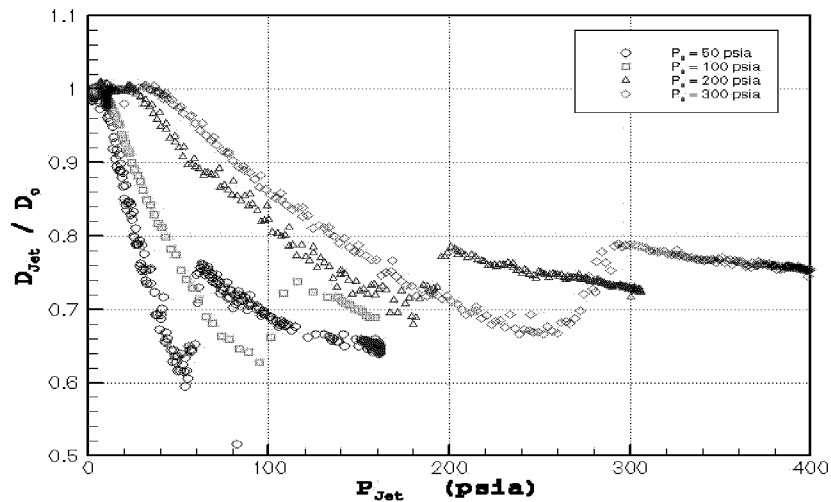


Figure 6. Drag measurements for different wind tunnel stagnation pressures

Non-Equilibrium Phenomenon

The injecting air plasma is generated by a plasma torch embedded within the model and issues from the stagnation point. In Figure 7, a composite picture of the model in the testing condition is depicted. The top half of the figure consists of the video image of the plasma torch in operation; the lower half of the composite is the schlieren of the same test. Overlaid is the sketch of the plasma torch. For the plasma generation in the starting mode of the torch, the power input is relatively low in comparison with the fully rated capacity of 7.28 kW. In order to be compatible with the energy input to the air supply of the torch, the stagnation pressure input to the torch has a limited operation range from 482.6 to 965.2 kPa. At the air supply stagnation temperature of 294 K and the stagnation pressure of 482.6 kPa to the plasma torch, the calculated mass-flow rate is 0.52 gm/sec. This injecting rate is small in comparison with the wind tunnel mass-flow rate of 0.77 kg/sec. Under the testing condition the counter-flow jet and shock interaction is in the subcritical state of shock bifurcation, and the entire flow field is in a self-sustained oscillatory motion. The measurement at a fixed point in space also collected data with wide range of temporal variation. Therefore, the measured data exhibited a large data scattering band.

The temperatures of internal degrees of freedom were determined by the optical emission from the positive electronic transition $C^3\pi_u \leftrightarrow B^3\pi_g$ of molecular nitrogen N_2 , and $C^2\pi_u^+ \leftrightarrow X^2\pi_g^+$ transition of the ionized

nitrogen N_2^+ [19,20]. A composite spectrum of the plasma torch in the 3400 to 4400 angstrom wavelength range stood out from the obscured by other emission from other species, such as the molecular oxygen, nitric oxide, as well as vapors of copper and iron. Therefore, the spectral match of the positive electronic transition of N_2 for rotational temperature cannot be performed. However, the averaged vibrational temperature, determined from the Boltzmann plot and a blackbody modeling, is 4400 ± 400 K. At the relatively high-pressure shock layer region, it would be reasonable to assume that the translational and rotational temperatures are equilibrated to the vibrational excitation. The electron temperature deduced from the langmuir double probe is around 20,000 K. Therefore, the only distinct temperatures are that of electron and the heavy particles [23,24]. The thermodynamic properties are similar to that reported in the works of Ganiev et al [6] and Malmuth et al [7].

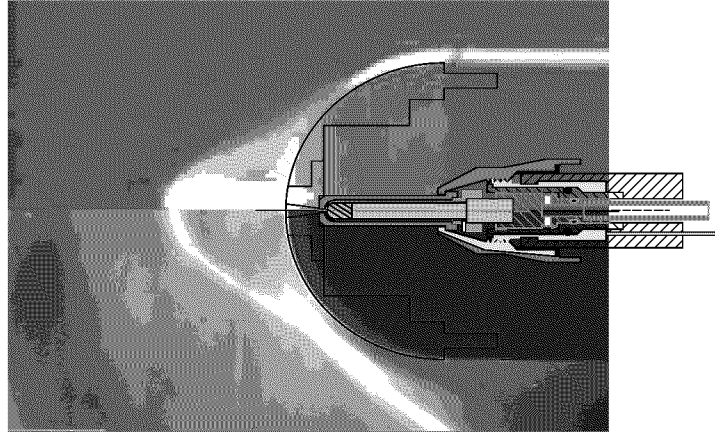


Figure 7. Composite presentation of the air plasma injection

At this temperature and static pressure within the shock layer of 10.5 kPa (78.9 Torr), the air plasma chemical composition in equilibrium condition can be determined from numerical data bases [22]. In term of mass fraction, N_2 , O, and NO have the value of 0.69, 0.26, and 0.5 respectively. As one may notice, the molecular oxygen is depleted from the air plasma mixture. The components of NO^+ , O^+ , N_2^+ , and N^+ are in the order of magnitude from 10^{-5} to 10^{-10} .

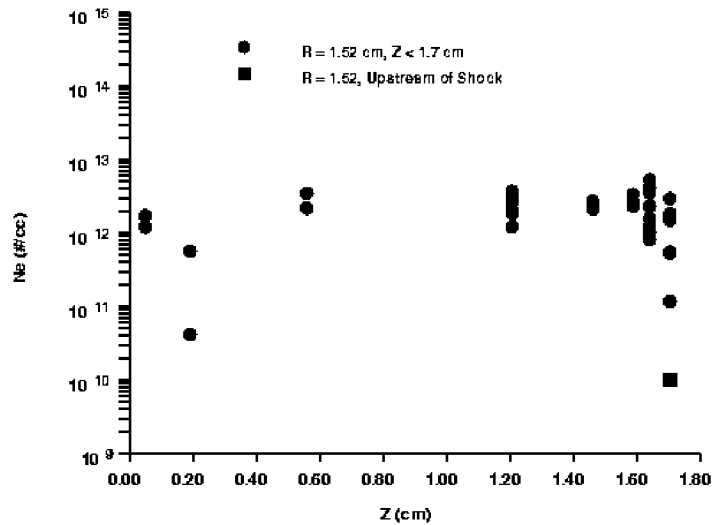


Figure 8. A typical measured electron number density in the shock envelope

The electron number density and electron temperature of the plasma were measured by a double Langmuir probe. The survey locations of the probe are restricted to the outer envelope of the high temperature jet

plume. The closest survey radial distance from the centerline of the plasma plume is 7.6 mm. In general, the electron number density, electron temperature, electrical conductivity, and field strength attain the maximum value in the plasma plume. This observation can easily be made by examining the electron density and electron temperature distributions along a fixed radial distance from the model's axis of symmetry.

Figure 8 displays the electron number density in the axial coordinate z , from the body surface to the bow shock along a fixed radial distance ($r = 7.6$ mm). This radial distance is also the minimum separation distance between the probe and the plasma torch so that the plasma plume will not thermally shatter the ceramic sleeve. The highest electron number density is around $5 \times 10^{12} / \text{cm}^3$. The sharp drop of the measured value indicates the bow shock location. The bow shock exhibits an oscillatory range from 21.2 to 24.6 mm from the blunt body surface. The electron number density upstream of the shock is less than 10^{10} , which is beyond the validated measurement range of the present probe capability.

The electron temperature distribution at corresponding location is presented in Figure 9. Again, the data scattering band is the greatest among all measurements within the entire shock layer envelope. Along the constant radial array, the calculated translational temperature is changing rapidly; the electron temperature is nearly constant to yield a value slightly higher than 20,000 K. Beyond the bow shock envelope, the electron temperature of the oncoming air falls below the value which can be measured with any certainty.

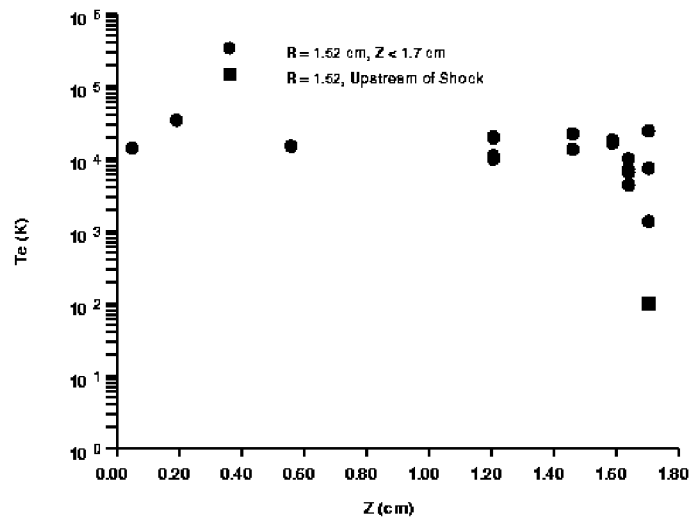


Figure 9. A typical measured electron temperature in the shock envelope

Although the injected air plasma has two distinct temperatures, but the chemical composition of highly excited species only present in trace amount. The plasma counter-flow jet is in a thermodynamically non-equilibrium state, the true species composition and internal energy partition at the present finitely can't be predicted with certainty [24]. Therefore, the detection of the non-equilibrium phenomenon is approached from a calculation based on a locally equilibrium chemical composition. The significance of non-equilibrium phenomenon to drag reduction is assessed through the departure from this state.

The plasma injection is evaluated by the mass-averaged, time-dependent Navier-Stokes equations without the aide of detailed chemical kinetics rates but with equilibrium air plasma composition. In addition, the vibrational temperature (4400 K) is assumed to be equilibrated with the translational and rotational degrees of freedom, but not with the electron temperature (20,000 K). From these stipulated conditions, the specific heat γ , deduced from the chemical equilibrium composition yields a value of 1.281. The comparison of the computed shock structures with the schlieren at an injection pressure of 582 kPa is depicted in Figure 10. It becomes clear that the computed shock structure using the equilibrium air plasma injection captures all essential features of the plasma jet interaction [25,26].

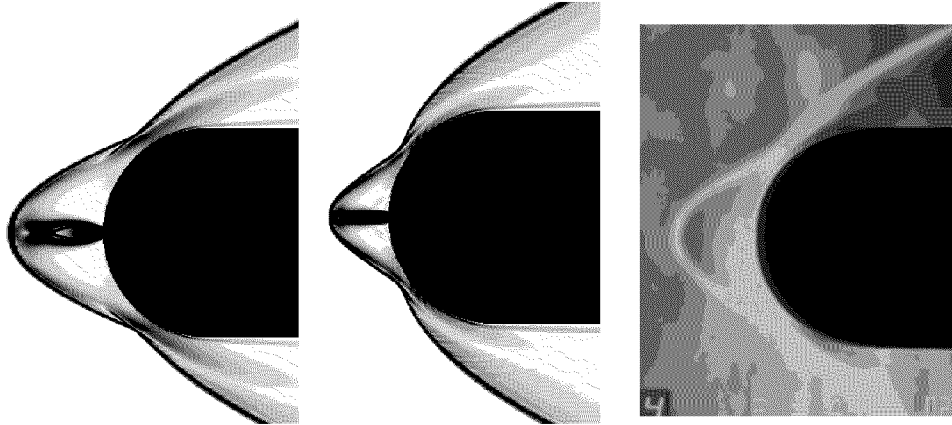


Figure 10. Comparison of schlieren and computation of plasma jet interaction

Figures 10 present two numerical results and a schlieren photograph. The left most image depicts the computed air injection with the perfect gas model at stagnation temperature of 300 K and the stagnation pressure of 582 kPa. The middle image is obtained by solving the Navier-Stokes equations with the equilibrium air plasma composition and at the stagnation temperature of 5280 K. At the numerical boundary of the sonic throat, the temperature then matches the experimental measurement of 4400 K. The computed result using the equilibrium chemical composition exhibits all flow field behaviors as observed in the experiment. When plasma torch is ignited, the overall shock wave system of air plasma injection retracted from the air injection at room temperature. The shock standoff distance of the computation attains a closer value to the experimental observation. Most importantly, the calculated drag agrees with data within a few percents as that of previous counter-flow jet interaction [14].

Analyzing all the computations based on perfect air and equilibrium air plasma composition, the retraction of shock wave system by the air plasma injection is mostly associated with a reduced mass flow rate by the elevated plasma temperature [25,26]. The mass flow rate of a nozzle is linearly proportional to the stagnation pressure, and inverse proportional to the square root of the stagnation temperature $m \sim (P_0/\sqrt{T_0})$. Therefore, at the investigated condition, the mass flow rate of the plasma injection is reduced by a factor of 3.9 from the room-temperature counterpart. For the present experimental process, the record of drag data starts with room temperature air injection. The plasma is then introduced by igniting the plasma torch and is sustained for a duration of 15 seconds. This realization of diminished mass flow rate of plasma injection succinctly explains the contradicting experimental observation that the measured drags actual rise when the plasma is ignited.

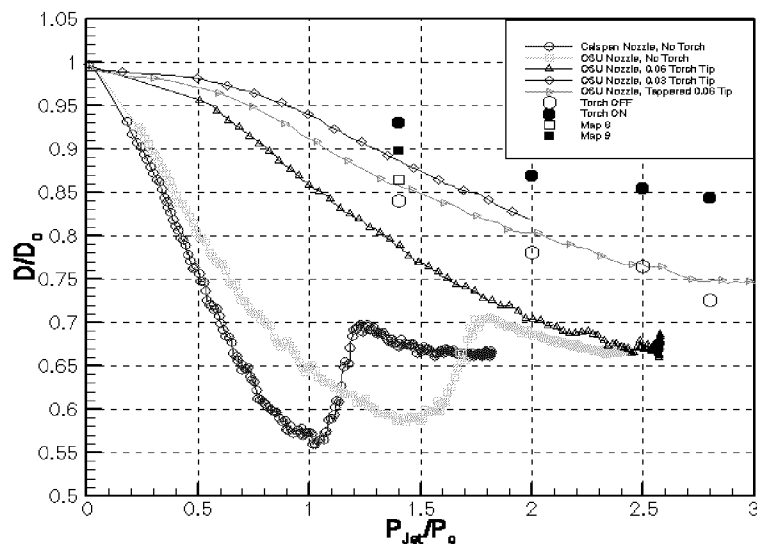


Figure 11. Drag data versus the ratio of plasma injection and tunnel stagnation pressures

In Figure 11, drag data of counter-flow jet from three different nozzles were included. However, the corresponding data of plasma injection is only obtainable at the smallest nozzle throat diameter of 1.27 mm. A single data point at the lowest injecting pressure also contained the effect of an applied magnetic field in the axial direction of the plasma chamber. Its significance will be discussed later.

The data of air injections were collected on different dates and by different procedures. One set of the data was collected by a data sweep for which the data is sampled at 500 points per second. Another set of data was collected in each individual test when plasma injection took place. These data sets indicated the scattering band of measurement about 3.5% over the entire tested range. In this graph, the drag of the blunt body with air plasma injection is reduced from the case when there is no injection, but the drag is greater than the air injection counter part. This erroneous perception is drawn from the incorrect interpretation of data in an inappropriate parametric space of stagnation pressures ratio rather than the mass flow rate.

The drag computations using equilibrium air plasma composition and perfect gas model are presented together with data in mass flow rate in Figure 12. The mass rate is normalized by the maximum air plasma injection rate achievable by the plasma torch. The calculated mass flow rate of 0.13, 0.19, 0.23, and 0.26 corresponds to injecting stagnation pressure ratios, P_j/P_0 of 1.4, 2.0, 2.5, and 2.8, respectively. Solutions of Navier-Stokes equations using the perfect gas model over the complete tested range are included as the point of reference. The overall agreement between computations and experiment is reasonable. Numerical results have a maximum discrepancy with the data of about 5% at the low injecting mass flow region. This quantification is believed to be the accuracy bound of the present investigation.

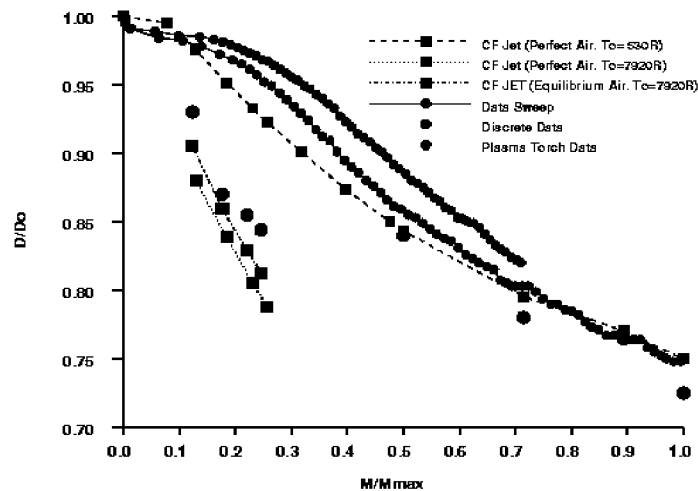


Figure 12. Comparison of computed and measured data of plasma injection

In this physically meaningful parameter of mass flow rate, the drag reduction via air plasma injection can be easily explained. First, at the identical mass flow rate, the air plasma injection indeed produces a greater drag reduction than its room-temperature counter part. The major portion of the reduced drag is derived from the thermal deposition of the air plasma. Based on the computational results using perfect gas and equilibrium air composition of the air plasma at the measured injecting conditions, the drag reduction diminishes for the latter. This observation is understandable in view of the fact that energy is redistributed among different internal degrees of freedom instead of the simple thermal to kinetic energy conversion process by the expansion. Finally, the numerical simulations using the chemical equilibrium composition of the air jet approach that of the data. The difference between computations and experiments is confined within the band of measurement uncertainty.

From the present investigation of air plasma injection from a blunt body, it is clearly demonstrated that the major portion of the drag reduction is derived from the counter-flow jet and shock interaction. The additional advantage of air plasma injection is gained from the thermal deposition. A higher thermal energy

content of the injected plasma leads to a lower required mass injection flow rate. In this sense, the air plasma injection is a more efficient drag reduction system. To achieve the same level of drag reduction, the mass flow rate of plasma injection is less than the air injection counterpart. However, the thermodynamic and chemical non-equilibrium effects in plasma injection are not directly assessable based on the state-of-the-art technique. From the present incremental analyses, these non-equilibrium phenomena under the tested condition are deemed not significant.

Electromagnetic effects

The first significant magneto-aerodynamic interacting phenomenon was demonstrated by the pioneering work of Ziemer [5]. He has shown that the shock standoff distance over a blunt body in a plasma stream increased drastically by an applied magnetic field. His pioneering work indicated that the standoff distance increased by a factor of 7.5 for an electromagnetic interaction parameter ($\sigma B^2 L / \rho u$) of 69. The electromagnetic force has been known to modify the Rankine-Hugoniot jump condition across a shock [2,23]. Taking it one step further, Shang has illustrated that the two additional entropy change mechanisms have been introduced by the electromagnetic field into the second law of thermodynamics across a one-dimensional normal shock [9].

$$\rho u \Delta s = \int (\kappa / T^2) (dT/dx)^2 dx + \int [(2\mu + \lambda) / T] (du/dx)^2 dx + \int J^2 / (\sigma T) dx - \int u (\mathbf{J} \times \mathbf{B})_x / T dx$$

The above equation clearly shows that the electromagnetic-aerodynamic interaction has the potential to reduce the wave drag for blunt body in supersonic flow. However to obtain the benefit of aerodynamic-electromagnetic interaction, the plasma medium must be introduced upstream of the shock and interacted with an applied electromagnetic field. To obtain the maximum effectiveness, the applied electromagnetic field is preferred in the transverse direction to the charge carrying flowing medium. These conditions were not met in all plasma injection experiments for drag reduction [7-9].

A single data point presented in Figure 11 has recorded a preliminary study of an applied magnetic field to the plasma injection. The applied magnetic field was imposed by a set of Neodymium rare earth (NeFeB) magnets around the plasma torch chamber. The applied field is aligned with the axis of the nozzle to enhance the plasma pinch effect. The magnet has a maximum magnetic flux density of 0.47 Tesla at the pole, but the field strength diminishes rapidly toward the nozzle axis. The estimated value is about 0.17 Tesla locally, the interaction parameter is uncertain far less than unity. This fact is verified by the observation, that the magneto-aerodynamic interaction is negligible. From this experimental setup, one observes that even if the electromagnetic field induced by the injecting plasma would reach the magnitude of the applied magnetic field, the interaction of magneto-aerodynamic interaction is still negligible.

Conclusions

The shock bifurcation phenomenon was discovered by a combined computational and experimental effort in analyzing the injecting plasma phenomenon. The shock structures of the counter-flow jet have two distinct dynamic states. In the sub-critical range, the flow field is in a self-sustained oscillatory motion. In the super-critical range, the entire flow field returns to the steady state. At the bifurcation point, the total aerodynamic force including the wave drag, skin-friction drag, base drag, and the reverse thrust of the counter-flow jet reaches the minimum value.

The present investigation reveals that the major portions of drag reduction by plasma injection are derived from the favorable shock and counter-flow-jet-shock interaction and thermal energy deposition. The non-equilibrium thermodynamics and chemical kinetics has insignificant effect. The contribution from the electromagnetic-aerodynamic interaction is negligible.

It may be interesting to note that an efficient combination of simulation technologies for risk and cost reduction is an actual reflection of the stage of maturation for each individual technology development. The present result also reveals the need for integrating computational fluid dynamics, electromagnetics, chemical kinetics, as well as, quantum chemical physics for future interdisciplinary application.

Acknowledgment

The author deeply appreciates the sponsorship by Drs. S. Walker and J. Schmiseur of the Air Force Office of Scientific Research. The invaluable contributions by Mr. J. Hayes, Dr. D. Emmer, Prof. J. Menart and the wind tunnel crew – T. Norris, R. Raber, and M. Greene – are duly acknowledged.

References

1. Shang, J.S., Assessment of Aeronautical Science for the 21st Century, Keynote Speech, Japan Society for Aeronautical and Space Science 37th Air Craft Symposium, Tokyo Japan, Oct 1999, Proceedings of JSASS 13th International Sessions, pp. 571-574.
2. Resler, E.L. and Sears, W.R., The Prospects for Magneto-aerodynamics, JAS Vol. 25, 1958, pp. 235-245 and 258.
3. Bush, W.B., Magneto-hydrodynamics-Hypersonic Flow Past a Blunt Body, J. Aero. Sci. Vol. 25, 1958, pp. 685-690 and 728.
4. Meyer, R.C., On Reducing Aerodynamic Heat Transfer Rates by Magneto-hydrodynamic Techniques, J. Aero/Space Sci. Vol. 6, 1958, pp.561-566 and 572.
5. Ziemer, Richard W., Experimental Investigation in Magneto-Aerodynamics, ARC J. Vol. 19, Sept. 1959, pp. 642-646.
6. Klimov A.I., Koblov A.N., Mishin G.I, Serov Yu. L., and Yavor, I.P., Shock Wave Propagation in a Glow Discharge, Sov. Tech. Phys Lett. Vol. 8, No. 4, 1982, pp.192-194.
7. Ganiev, Y.C., Gordeev, V.P., Krasilnikov, A.V., Lagutin, V.I., Otmennikov, V.N., and Panasenko, Aerodynamic Drag Reduction by Plasma and Hot-Gas Injection, J. Thermophysics and Heat Transfer, Vol. 14, No. 1, 2000, pp. 10-17.
8. Malmuth N.D., Fomin, V.M., Maslov, A.A, Formichev, V.P., Shashkin, A.P., Korotaeva, T.A., Shipyuk, A.N., and Pozdnyakov, G.A., Influence of a Counterflow Plasma Jet on Supersonic Blunt Body Pressures, AIAA 99-4883, the Third Weakly Ionized Gases Workshop, Norfolk VA, Nov. 1999.
9. Shang, J.S., Recent Research in Magneto-Aerodynamics, Progress in Aerospace Sciences, Vol. 37, 2001, pp.1-20.
10. Adamson, T.C., and Nicholls, J.A., On the Structure of Jet From Highly Under Expanded Nozzles into Still Air, J. Aero. Science, Vol. 26, 1959, pp. 16-21.
11. Baron, J.R., and Alzner, E., An Experimental Investigation of a Two Layer Inviscid Shock Cap Due to Blunt Body Nose Injection, J. Fluid Mech, Vol. 15, 1963, pp.400-412.
12. Finley, P.J., The Flow of a Jet from a Body Opposing a Supersonic Free Stream, J. Fluid Mech., Vol. 26, Part 2, 1966, pp. 337-368.
13. Barber, E. A. Jr., An Experimental Investigation of Stagnation-Point Injection, J. Spacecraft, 1955, pp.770-774.
14. Shang, J.S., Hayes, J.R., Wurtzler, K., and Strang, W., Jet-Spike Bifurcation in High-Speed Flows, AIAA J., Vol. No.6, June 2001, pp. 1159-1165.
15. Rockwell, D., and Naudascher, E., Self-Sustained Oscillations of Impinging Free Shear Layers, Annual Review of Fluid Dynamics, Vol. 11, Annual Review, Inc., Palo Alto CA, pp. 67-94, 1979
16. Strang, W.Z., Tomaro, R.F., and Grismer, M., The Defining Methods of Cobalt: A Parallel, Implicit, Unstructured Euler /Navier-Stokes Flow Solver, AIAA 99-0786, January 1999.
17. Grismer, M.J., Strang, W.Z., Tomaro, R.F., and Witzeman, F.C., Cobalt: A Parallel, Implicit, Unstructured Euler/Navier-Stokes Solver, Advances in Engineering Software, Vol. 29, 1998, pp.365-373.
18. Sparat, P.R. and Allmaras, S.R., A One-equation Turbulent Model for Aerodynamic Flows, AIAA 92-0439, January 1992.
19. Shang, J.S., Ganguly, B., Umstatted, R., Hayes, J., Arman, M., and Blitzenger, P., Developing a Facility for Magneto-aerodynamic Experiments, J. Aircraft, Vol. 17, No. 6, 2000, pp. 1065-1072.
20. Gilmore, Forrest R., Laher, Russ R., and Espy, Patrick J., Franck-Condon Factors, r-Centroid, Electronic Transition, Moments, and Einstein Coefficients for Many Nitrogen and Oxygen Band Systems, J. Phys. Chem. Rev. Data, Vol. 21, No. 5, 1992, pp.1005-1107.

21. Huber, K.P. and Herzberg, G., *Molecular Spectra and Molecular Structure, Vol. IV: Constants of Diatomic Molecules*, Van Nostrand Reinhold Co., 1979.
22. McBride, B.J. and Gordon S., *Computer Program for Calculation of Complex Chemical Equilibrium Compositions and Applications, II. User Manual and Program Description*, NASA Ref. Pub. 1331 June 1996.
23. Mitchner, M. and Kruger, C.H., *Partially Ionized Gases*, John Wiley and Sons, NY, 1973, pp.163-241.
24. Park, C., *Assessment of Two-Temperature Kinetic Model for Ionizing Air*, AIAA 87-1574. 1987
25. Shang, J.S., Hayes, J.R., and Menart, J.A., *Hypersonic Flow over a Blunt Body with Plasma Injection*, AIAA 2001-0344, Reno NV, January 2001.
26. Shang, J.S., Hayes, J.R., Miller, J.H., and Menart, J.A., *Blunt body in Hypersonic Electromagnetic Flow Field*, AIAA 2001-2803, Anaheim CA, June 2001.